Secondary-Side-Regulated Soft-Switching Full-Bridge Three-Port Converter Based on Bridgeless Boost Rectifier and Bidirectional Converter For Multiple Energy Interface

Hongfei Wu, *Member*, *IEEE*, Junjun Zhang, Xiaoqing Qin, Tiantian Mu, Yan Xing, *Member*, *IEEE*

***Abstract*—A systematic method for deriving soft-switching three-port converters (TPCs), which can interface multiple energy, is proposed in this paper. Novel full-bridge (FB) TPCs featuring single-stage power conversion, reduced conduction loss and low voltage stress are derived. Two non-isolated bidirectional power ports and one isolated unidirectional load port are provided by integrating an interleaved bidirectional Buck/Boost converter and a bridgeless Boost rectifier via a high frequency transformer. The switching bridges on the primary side are shared, hence the number of active switches is reduced. Primary-side pulse width modulation and secondary-side phase shift control strategy are employed to provide two control freedoms. Voltage and power regulations over two of the three power ports are achieved. Furthermore, the current/voltage ripples on the primary-side power ports are reduced due to the interleaving operation. Zero-voltage-switching and zero-current-switching are realized for the active switches and diodes, respectively. A typical FB-TPC with voltage-doubler rectifier developed by the proposed method is analyzed in detail. Operation principles, control strategy and characteristics of the FB-TPC are presented. Experiments have been carried out to demonstrate the feasibility and effectiveness of the proposed topology derivation method.**

***Index Terms*—DC-DC converter, three-port converter, renewable energy, bridgeless boost rectifier, secondary-side regulation.**

I. Introduction

STORAGE battery capable of long-term energy buffering has been a critical element in renewable power systems due to the intermittent nature of sustainable energy [1][2]. Renewable energy power systems need to interface several energy sources such as photovoltaic (PV) array, fuel cells with the load along with a battery backup. A three-port converter (TPC) finds applications in such systems, because it has multiple interfacing ports and can accommodate a primary source and a storage and combines their advantages by utilizing a single power stage[3][4]. In comparison with using multiple traditional two-port converters, the most attractive features of using a TPC are reduced power conversion stages and reduced component count. Hence the efficiency and power density are improved and the cost is reduced[5]. Due to its advantages, the TPC is continuously evolving and new topologies and innovations have been continuously emerging [5]-[23].

The search for TPC topologies with simpler design, higher efficiency and better control performance is a significant driving force in the power electronics research community. Component sharing and circuit integration are key techniques for deriving TPC topologies. Following this principle, many TPC topologies were reported in [3]-[23]. These TPC topologies can be classified into three categories: non-isolated TPCs[6]-[9], fully isolated TPCs[10]-[12], and partially isolated TPCs[13]-[23]. The partially isolated TPCs, which are the main focus of this paper, combine the advantages of the non-isolated and fully isolated TPCs. They can realize high efficiency non-isolated power conversion between the primary source and storage battery, while provide necessary isolation and flexible voltage level for the load port. Besides, active switches are shared and soft-switching can be achieved to realize high efficiency.

Due to their remarkable merits, many partially isolated TPCs have been invented, proposed, and demonstrated for various applications, such as distributed renewable power system[13], electric vehicles[14], stand-alone renewable power system[16]-[19], etc.. A flyback TPC is presented for a micro-inverter [15]. Compared to a traditional flyback converter, the time-sharing control scheme couples the primary-side power ports and limits the flexibility of energy delivery. A tri-modal half-bridge TPC is proposed by integrating the half-bridge and active-clamp forward topologies [16]. Two families of half-bridge TPCs with synchronous regulation and post-regulation are proposed [17]. These half-bridge TPCs have some obvious advantages in terms of saving cost and component count, and simplifying structure and power management. However, in comparison with the traditional two-port half-bridge converter, the efficiency is decreased because additional conduction losses are introduced by the free-wheeling operating stage[16][17]. Moreover, it is difficult to decouple the power control loops and design optimized compensators for the three power ports [18]. Because the voltage and power of all of the three power ports are regulated by the same control variables, the duty cycles of the two primary-side switches. By integrating non-isolated Buck, Boost, or Buck-Boost converters into the phase-shift

Manuscript received Feb. 08, 2015, revised June 23, 2015, accepted Aug. 18, 2015. This work was supported in part by the National Natural Science Foundation of China under Grant 51407092 and 51377083, in part by Foundation of State Key Lab of Power System(SKLD15KZ01), in part by grants from the Power Electronics Science and Education Development Program of Delta Environmental & Educational Foundation (DREG2014012), and in part by the Natural Science Foundation of Jiangsu Province, China under Grant BK20140812.

The authors are with the Jiangsu Key Laboratory of New Energy Generation and Power Conversion, College of Automation Engineering, Nanjing University of Aeronautics and Astronautics, Nanjing 210016, China (e-mail: wuhongfei@nuaa.edu.cn).

full-bridge (FB) converters, several types of full-bridge TPCs are proposed in [19]-[23]. Active switches are shared and zero-voltage-switching (ZVS) is achieved with these FB TPCs. What's more, approximately decoupled power control is realized by applying PWM plus phase-shift control strategy [21][22]. However, there are some disadvantages in common due to the primary-side modulation scheme and the phase-shift FB topology. These disadvantages are summarized as follows: 1) higher current and voltage ripples on the three power ports because the two switching-bridges on the primary side cannot be driven in an interleaved fashion (with 180° phase shift); 2) additional conduction losses caused by the circulating current during the freewheeling stage; 3) high voltage spikes and severe reverse recovery losses of the secondary rectifying diodes; 4) low duty cycle utilization ratio due to duty cycle loss. To overcome these drawbacks of previous TPCs, novel solutions are proposed in this paper.

The major contribution of this paper is to propose a systematic approach for deriving novel full-bridge three-port converters based on integration of an interleaved bidirectional converter and bridgeless boost rectifiers. A new family of FB TPCs with PWM plus secondary-side regulation control strategy is proposed. The proposed topology has the following advantages: 1) single-stage power conversion and approximately decoupled control between any two of the three ports are achieved; 2) ZVS and zero current switching (ZCS) are achieved for active switches and diodes, respectively; 3) input current ripple is reduced thanks to the interleaving operation, which is beneficial for ripple sensitive power sources; 4) the freewheeling current is effectively suppressed and the voltage spikes on the secondary-side switches are eliminated. This paper is organized as follows. In section II, the basic ideas to generate novel FB TPCs are proposed with a family of FB TPCs harvested. A FB TPC with voltage-doubler rectifier is taken as an example being analyzed in detail to verify the proposed method in Section III and Section IV. Experimental results are presented in Section V. Finally, conclusion will be given in Section VI.

II. Derivation of the FB TPC From Bidirectional Converter and Bridgeless Boost Rectifiers

The structure of the proposed FB TPC is shown in Fig. 1. Two bidirectional Buck/Boost converters are employed to interface two bidirectional power ports on the primary-side of the FB TPC. The two switching legs, composed of S_1, S_2 and S_3, S_4, of the two bidirectional Buck/Boost converters are driven in the interleaved fashion (with 180° phase shift). From a topological point of view, the two switching-legs also build a voltage-fed full-bridge inverter. A high frequency AC voltage, v_P, is generated from the mid-points of the two switching-legs.

It has been well-known that, an AC voltage can be converted to a regulated DC voltage efficiently by employing a bridgeless Boost rectifier, because the conduction loss and the number of semiconductor components are reduced [24]-[27]. This drops a hint that another controllable power port can be built by using a bridgeless Boost rectifier to rectify the afore-mentioned AC voltage to a regulated DC voltage. Furthermore, to provide necessary isolation and flexible voltage level for this power port, a high-frequency transformer can be inserted between the

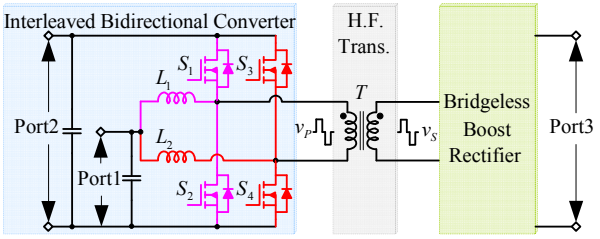

Fig. 1. Structure of the proposed FB TPC based on an interleaved bidirectional converter and a bridgeless Boost rectifier.

interleaved bidirectional Buck/Boost converter and the bridgeless Boost rectifier. As a result, as shown in Fig. 1, the structure of the proposed FB TPC is composed of three parts: an interleaved bidirectional Buck/Boost converter, a high-frequency transformer, and a bridgeless Boost rectifier.

There are many candidate topologies for the bridgeless Boost rectifier. Some of the possible choices for the bridgeless Boost rectifier topologies are shown in Fig. 2. A family of novel FB TPC topologies can be derived by replacing the block diagram on the secondary-side of Fig. 1 with the circuits in Fig. 2. Two example topologies, which are derived from the bridgeless Boost rectifiers in Fig. 2(a) and Fig. 2(f), respectively,are illustrated in Fig. 3.

It should be noted that the proposed FB TPC is not a simple combination of the bidirectional converter and the Boost rectifier. In comparison with the traditional bridgeless Boost rectifier which processes line frequency voltage, the Boost rectifier in the proposed FB TPC is used to process high frequency voltage. So the operation principles, control strategies and characteristics will be totally different. Close observation indicates that the proposed FB TPCs have the following features:

1) The FB TPC has two bidirectional power ports and one isolated output port. The two bidirectional ports can be used to interface renewable energy sources, storage elements, regenerative DC loads or voltage buses with bidirectional power flows, whereas, the isolated output port can only be used to interface DC load or voltage bus with an unidirectional power flow.

2) Single-stage power conversion between any two of the three ports is achieved. The voltage and power of Port1 and Port2 on the primary side can be balanced by regulating the duty cycle of the bidirectional Buck/Boost converter, while the output voltage/power of the Port3 on the secondary-side can be controlled by the bridgeless Boost rectifier. Therefore, tight control over two of the three ports can be achieved while the third port provides the power balance for the system.

3) Low voltage/current ripples on the primary-side power ports can be ensured because the two bidirectional Buck/Boost converters always operate with an interleaving fashion.

4) Low voltage stresses on all of the power devices can be realized because all the devices can be clamped by the input and output voltages directly. Especially, for the three-level Boost rectifiers such as those shown in Fig. 2(d)~(f), the active switches on the secondary-side only suffer from half of the output voltage.

5) The leakage inductance of the high-frequency transformer can be used as part of the Boost inductor, which means the

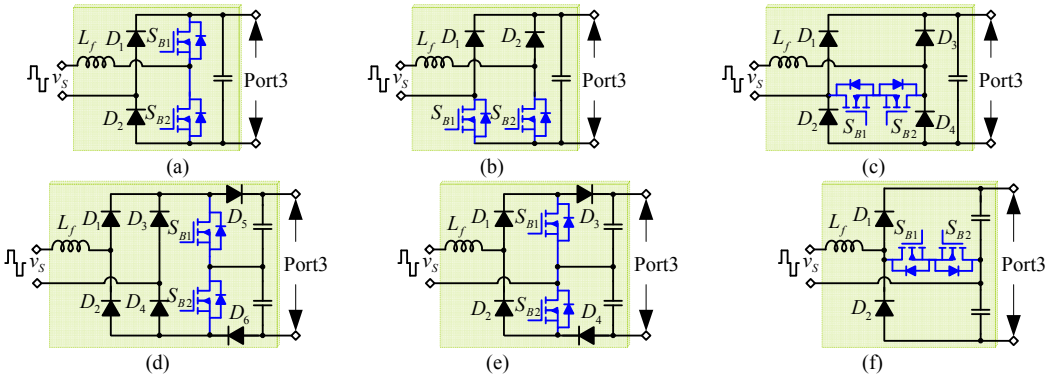

Fig. 2. Candidate topologies of bridgeless Boost rectifiers, (a)~(c) full-bridge, (d)~(e) three-level.

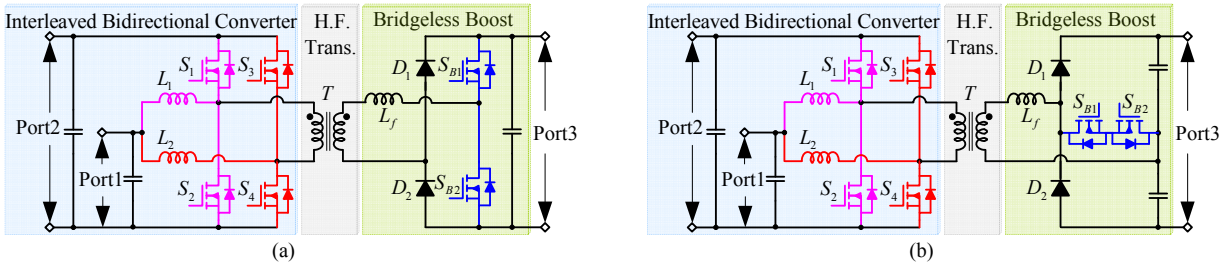

Fig. 3. Example topologies of the proposed FB TPC, (a) with full-bridge rectifier, (b) with voltage doubler rectifier.

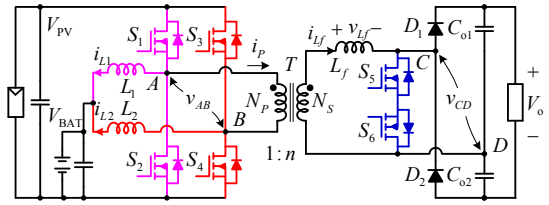

Fig. 4. Topology of the proposed FB-TPC.

parasitic parameter of the transformer can be utilized effectively.

III. Operational Principles of the FB-TPC with Voltage Doubler

The FB-TPC with a voltage-doubler rectifier, as shown in Fig. 3(b), is taken as an example to verify the proposed topology derivation method and derived topologies. This FB-TPC is applied to an aerospace power system, which is a typical stand-alone renewable power system sourced by PV and battery. The Port1, Port2 and Port3 of the FB-TPC are connected to a battery, a PV source and an isolated load, respectively. To better analyze the operation principle, the proposed topology is redrawn in Fig. 4.

Power flow paths from the PV to the load, from the PV to the battery and from the battery to the load have been built by the FB-TPC. The equivalent circuit of each power flow path is illustrated in Fig. 5. Ignoring the power losses in the conversion, we have

$$p_{PV} = p_{BAT} + p_o \tag{1}$$

where p_{PV}, p_{BAT} and p_o are the power flowing through the PV source, the battery and the load, respectively. When $p_{PV} \geq p_o$, the battery is charged and absorbs the surplus PV power, and both the load and battery take power from the PV. When $p_{PV} < p_o$, the battery will discharge and supply power along with the PV. Once p_{PV} is zero, all of the load power is provided by the battery.

From the standpoint of power control, two of the three power ports should be controlled simultaneously while the third one is used for power balance. The duty cycle of the primary side switches is employed to balance the voltage and power between the PV and the battery, that is to realize maximum power point tracking of the PV source or charging control of the battery. The phase shift angle φ between the primary and secondary side switches is employed to regulate the output voltage and provide another control freedom for the load port. The power control of the primary side power ports is independent of the secondary-side load port. Because the duty cycle of the primary-side switches is only determined by the voltages of the battery and the PV source, and has nothing to do with the phase shift angle φ.

The key waveforms of the primary-side interleaved Buck/Boost converter are illustrated in Fig.6, where D is the duty cycle of the switches S_1 and S_3, and T_s is the switching period. The switches in the same switching-leg are driven complementary, and the phase angle between the two switching-legs is 180° as constant to reduce the current ripple and enhance the circuit reliability. Since the operation of the interleaved bidirectional Buck/Boost converter is very simple, it will not be analyzed in detail in this paper. The operation of the proposed converter mainly focuses on the power flow from the primary-side to the load side.

According to the current waveform of the secondary-side Boost inductor, L_f, the FB-TPC has three possible operation modes, namely continuous conduction mode (CCM), discontinuous conduction mode 1 (DCM1) and discontinuous conduction mode 2 (DCM2), respectively. In order to simplify the analysis, normalized voltage gain, G, from the PV port to the load port is defined as

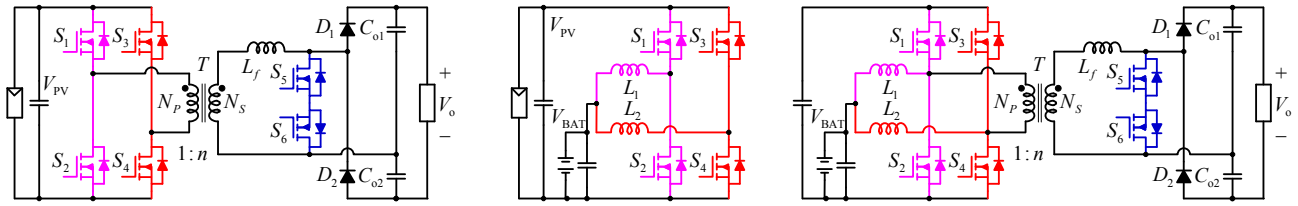

Fig. 5. Equivalent circuit of the three power flow paths in the proposed FB-TPC: (a) PV to load, (b) PV to battery and (c) battery to load.

$$G = \frac{V_o}{2nV_{PV}} \tag{2}$$

where V_{PV}, V_o and n are the PV voltage, load voltage and transformer turns ratio ($n = n_S / n_P$), respectively.

1) CCM

The converter operates in the CCM if the primary side switches commute before the secondary side inductor current, i_{Lf}, decreases to zero. The key waveforms of the CCM mode are shown in Fig.7, where v_{AB} and v_{CD} are the voltage differences between the midpoint primary and secondary side bridges, v_{Lf} and i_{Lf} are the voltage and current of the Boost inductor L_f, φ is the phase shift angle between S_1 and S_6, and α is defined to be the equivalent phase angle during which the primary side current returns to zero after S_1 turns on. $\varphi \geq \alpha$ is satisfied in the CCM. There are six stages in half of the switching period. The equivalent circuit of each switching stage is illustrated in Fig.8.

Stage 1 [t_0~t_1] [Fig.8(a)]: Before t_0, S_2, S_4 and S_5 are ON, the Boost inductor current i_{Lf} flows reversely. At t_0, S_2 is turned OFF. The body diode of S_1 begins to conduct due to the energy stored in L_f. In this stage, the inductor current i_{Lf} is expressed as follows.

$$i_{Lf}(t) = \frac{V_o/2}{L_f}(1/G+1)(t_1 - t_0) + i_{Lf}(t_0) \tag{3}$$

Stage 2 [t_1~t_2] [Fig.8(b)]: At t_1, S_1 is turned ON with ZVS, because the drain-source voltage of S_1 has decreased to zero due to the conduction of its body diode. This stage ends when i_{Lf} decreases to zero and D_2 is OFF naturally without reverse-recovery. The time interval ΔT_{20} is calculated by the following equation.

$$\Delta T_{20} = t_2 - t_0 = -\frac{2L_f i_{Lf}(t_0)}{V_o(1/G+1)} \tag{4}$$

So the phase angle α in the CCM is

$$\alpha_{CCM1} = 2\pi f_s \Delta T_{20} \tag{5}$$

where f_s is the switching frequency.

Stage 3 [t_2~t_3] [Fig.8(c)]: At t_2, i_{Lf} reaches zero. Since S_5 is ON, S_5 and the body diode of S_6 make up of one current loop, through which the Boost inductor current flows. Therefore, L_f is charged by the power sources on the primary-side, and i_{Lf} increases linearly due to the positive voltage across the inductor L_f. In this stage, the current i_{Lf} is calculated as

$$i_{Lf}(t) = \frac{V_o/2}{GL_f}(t - t_2) \tag{6}$$

Stage 4 [t_3~t_4] [Fig.8(d)]: At t_3, S_5 is turned OFF, and S_6 is turned ON with zero voltage, because the drain-source voltage of S_6 is zero due to the conduction of its body diode. Since the current of L_f is positive, the diode D_1 begins to conduct, and the power is transferred to the load. In this stage, the current i_{Lf} is expressed as follows.

$$i_{Lf}(t) = \frac{V_o/2}{L_f}(1/G-1)(t - t_3) + i_{Lf}(t_3) \tag{7}$$

Stage 5 [t_4~t_5] [Fig.8(e)]: At t_4, S_1 is turned OFF, and the body diode of S_2 is ON. The primary-side current begins to circulate through S_2 and S_4. The secondary current deceases due to the negative voltage across L_f.

$$i_{Lf}(t) = \frac{-V_o/2}{L_f}(t - t_4) + i_{Lf}(t_4) \tag{8}$$

Stage 6 [t_5~t_6] [Fig.8(f)]: At t_5, S_2 is turned ON with ZVS because the body diode of S_2 is in on-state. At the end of this Stage, i_{Lf} has the same absolute value but reverse direction as that at the beginning of Stage 1, which is expressed as

$$i_{Lf}(t_6) = -i_{Lf}(t_0) \tag{9}$$

A similar operation works in the rest stages of the switching period, with the roles of S_1 and S_2, S_3 and S_4, D_1 and D_2, S_5 and S_6 exchanged.

2) DCM1

In the DCM1, the primary-side upper switches, S_1 and S_3, commute after the secondary-side inductor current i_{Lf} decreases to zero, while the lower switches, S_2 and S_4, commute before i_{Lf} decreases to zero. The key waveforms of this mode are shown in Fig.9, where β is the effective phase angle during which i_{Lf} is not zero. There are also six stages in half of a switching period.

Stage 1 [t_0~t_1]: Before t_0, S_2, S_4 and S_5 are ON, and both D_1 and D_2 are OFF. There is no power being transferred to the load, because the current i_{Lf} has decreased to zero. At t_0, S_2 is turned OFF, the states of S_1 and S_2 depend on the direction of battery current. If the batter is charged, the current of L_1 will be positive. In this case, the body diode of S_2 keeps ON even when S_2 is turned OFF. The equivalent circuit of this case is shown in Fig.10 (a). However, if the battery is discharged, the current of L_1 is negative. The body diode of S_1 will be ON and the equivalent circuit is the same as that in Fig.8(a).

Stage 2[t_1, t_2]: The operation principles and equivalent circuit of the Stage 2 in the DCM1 are the same as that of Stage 3 in the CCM. At the end of this stage, the inductor current i_{Lf} is calculated as follows.

$$i_{Lf}(t) = \frac{V_o/2}{GL_f}\frac{\varphi/2\pi}{f_s} \tag{10}$$

Stage 3[t_2, t_3], Stage 4[t_3, t_4] and Stage 5[t_4, t_5]: The operation principles and equivalent circuits of the Stage 3, Stage 4 and Stage 5 in the DCM1 are the same as that of Stage 4, Stage 5 and Stage 6 in the CCM, respectively.

At the end of Stage 5, the inductor current i_{Lf} reaches zero, and the diode D_1 is OFF with zero current and without reverse recovery.

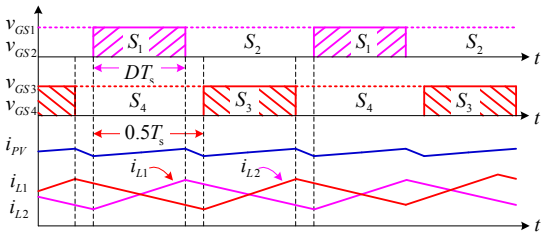

Fig.6. Key waveforms of the primary-side interleaved bidirectional Buck/Boost converter.

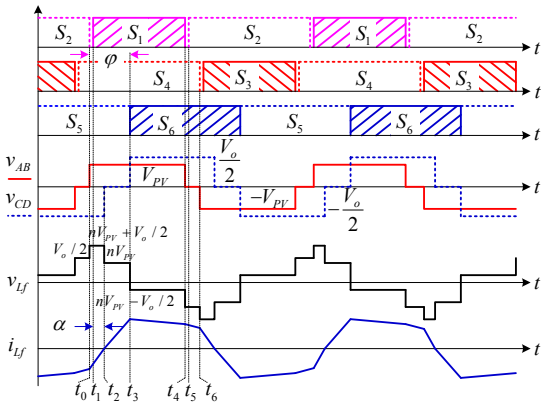

Fig. 7. Key waveforms of FB-TPC in the CCM.

Applying the volt-second balance principle on the inductor L_f, the time interval during which the inductor current i_{Lf} is not zero can be calculated by the following equation.

$$\Delta T_{51} = t_5 - t_1 = \frac{D/G + \varphi/2\pi}{f_s} \tag{11}$$

The equivalent phase angle β corresponding to ΔT_{51} is given by

$$\beta_{DCM1} = 2\pi f_s \Delta T_{51} \tag{12}$$

The maximum phase angle β is π, so the boundary phase shift angle between CCM and DCM1 modes is derived as:

$$\varphi_{b1} = \pi \frac{G - 2D}{G} \tag{13}$$

Stage 6[t_5, t_6]: At t_5, i_{Lf} reaches zero and will stay zero during this stage. In this case, there is no energy being transferred from the primary-side power sources to the load.

After t_6, a similar operation works in the rest stages of the switching period.

3) DCM2

The converter will operate in the DCM2 if the secondary-side inductor current i_{Lf} has decreased to zero before the primary-side switches, S_1~S_4, commute. The key waveforms of this mode are shown in Fig.11. There are also six stages in half of a switching period.

Stage 1[t_0, t_1], Stage 2[t_1, t_2] and Stage 3[t_2, t_3]:The operation principles and equivalent circuits of the Stage 1, Stage 2 and Stage 3 in the DCM2 are the same as that of the corresponding switching Stages in the DCM1.

At the end of Stage 3, the inductor current i_{Lf} decreases to zero. According to the volt-second balance principle of the inductor L_f, the time interval ΔT_{31} is calculated by the following equation.

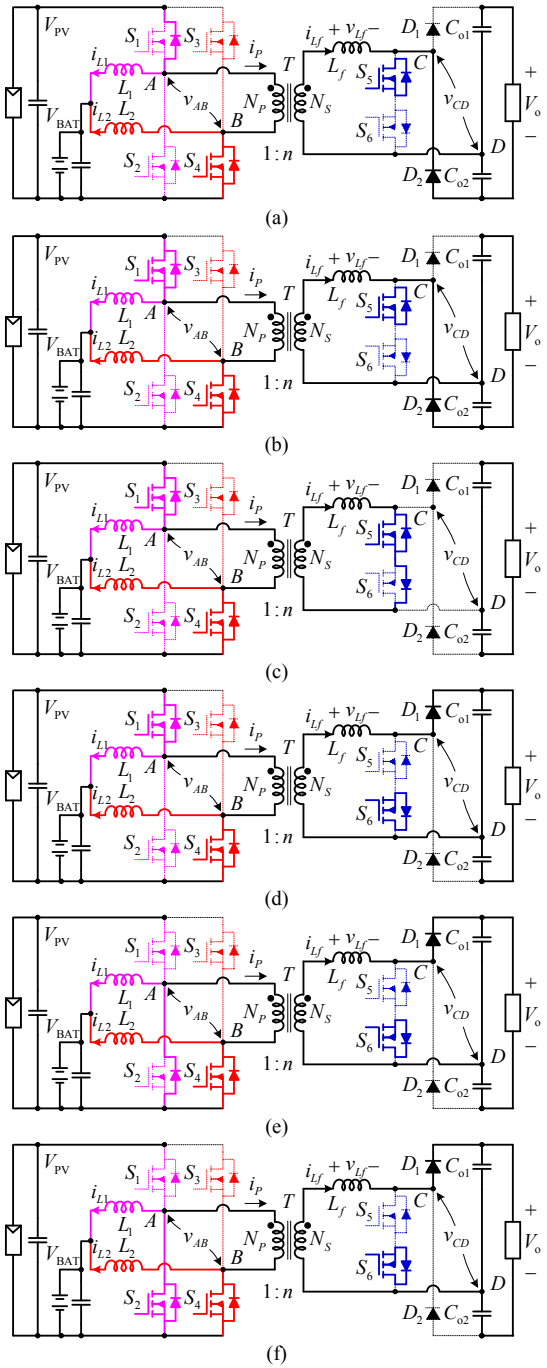

Fig.8. Equivalent circuits in the CCM: (a) Stage 1 [t_0~t_1], (b) Stage 2 [t_1~t_2], (c) Stage 3 [t_2~t_3], (d) Stage 4 [t_3~t_4] , (e) Stage 5 [t_4~t_5], (f) Stage 6 [t_5~t_6].

$$\Delta T_{31} = t_3 - t_1 = \frac{\varphi}{2\pi f_s \left(1 - 1/G\right)} \tag{14}$$

The maximum value ofΔT_{31} is D/f_s, therefore, the boundary phase-shift angle between DCM1 and DCM2 is derived as:

$$\varphi_{b2} = \frac{2\pi D\left(G-1\right)}{G} \tag{15}$$

Stage 4[t_3, t_4]: At t_3, i_{Lf} reaches zero. The diode D_1 is OFF without reverse recovery, hence ZCS is achieved for D_1. In this stage, there is no power being transferred from the primary-side

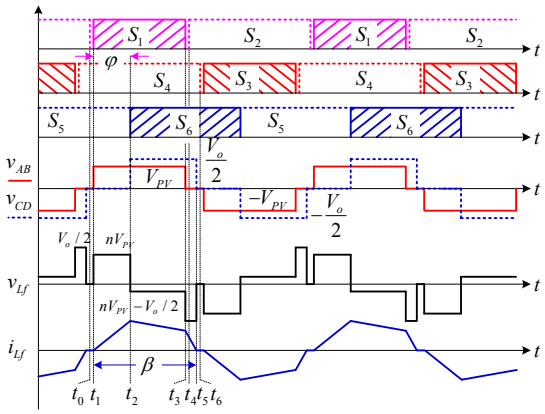

Fig. 9. Key waveforms of FB-TPC in the DCM1.

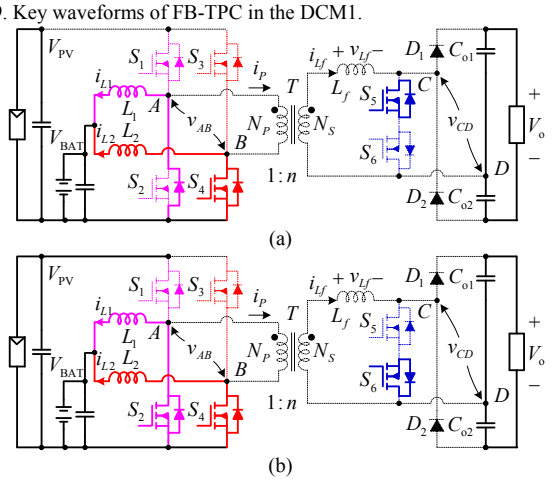

Fig. 10. Equivalent circuit in DCM1: (a) Stage 1 [t_0~t_1], (b) Stage 6 [t_5~t_6].

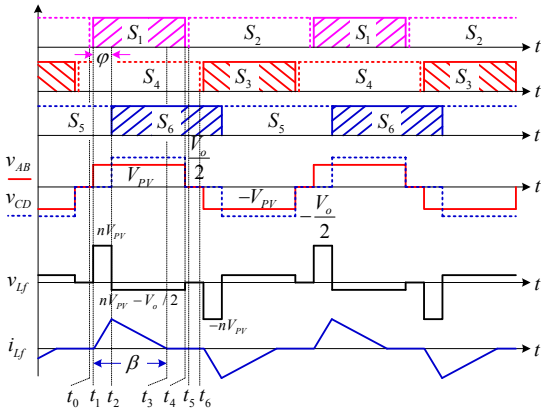

Fig. 11. Key waveforms of the FB-TPC in DCM2.

power sources to the load. The equivalent circuit of this Stage is shown in Fig. 12(a).

Stage 5 [t_4, t_5]: At t_4, S_1 is turned OFF. The status of the switches S_1 and S_2 depend on the battery. If the battery is charged, the current of L_1 is positive. In this scenario, the body diode of S_2 will be ON, and the switch S_2 can be turned ON with ZVS in the next Stage. The equivalent circuit of this case is shown in Fig. 12(b). However, if the battery is discharged and the current of L_1 is negative, the body diode of the switch S_1 will keep in ON state when S_1 and S_2 are turned-OFF. The equivalent circuit of this case is shown in Fig. 12 (c).

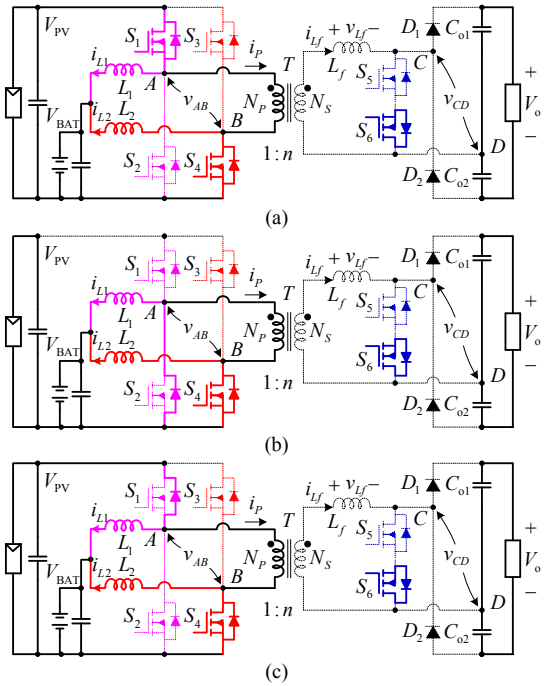

Fig. 12. Equivalent circuits of DCM2: (a) Stage 4 [t_3~t_4], (b) Stage 5 [t_4~t_5] when battery is charged, (c) Stage 5 [t_4~t_5] when battery is discharged.

Stage 6 [t_5, t_6]: The operation principle and equivalent circuit of this Stage is the same as that of the Stage 6 in the DCM1.

After t_6, a similar operation works in the rest stages of the switching period.

IV. Characteristics And Analysis

A. Output Characteristic

According to the aforementioned analysis of the CCM, the average current of the secondary-side Boost inductor is calculated by the following equation.

$$I_{av}=\frac{i_{Lf}(t_3)(\varphi-\alpha)}{2\pi}+\frac{\left[i_{Lf}(t_3)+i_{Lf}(t_4)\right](2\pi D-\varphi)}{2\pi} \tag{16}$$

Ignoring the power losses, the output power P_o can be given by:

$$P_o=P_{in}=nV_{PV}I_{av} \tag{17}$$

To simplify the analysis, the output power P_{out} is normalized with the power base P_B

$$P_B=\frac{V_o^2}{8\pi f_s L_f} \tag{18}$$

From (2)-(9) and (16)-(18), the normalized output power can be calculated and derived with the help of calculation software, such as MATHCAD. The derived output power of the CCM is given as follows.

$$P_{o\_CCM}=P_B\cdot\frac{\left[(8D-12D^2)(G+1)-\left(4D^2+1\right)G^2\right]\pi^2+\left[\left(8D+4\right)G^2+16D(G+1)\right]\pi\varphi-4\left(G+1\right)^2\varphi^2}{2G\left(2+G\right)^2\pi} \tag{19}$$

According to the operation principles of the DCM1 and DCM2, the output power of the DCM1 and DCM2 can be derived and expressed as follows.

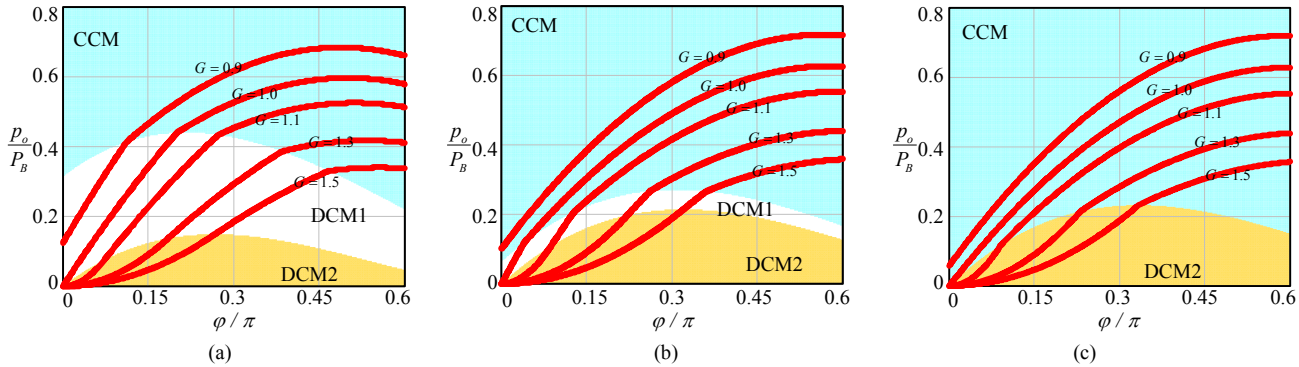

Fig. 13. Normalized output power versus secondary-side phase-shift angle with different primary-side duty cycle D, (a) D=0.4, (b) D=0.48, (c) D=0.5.

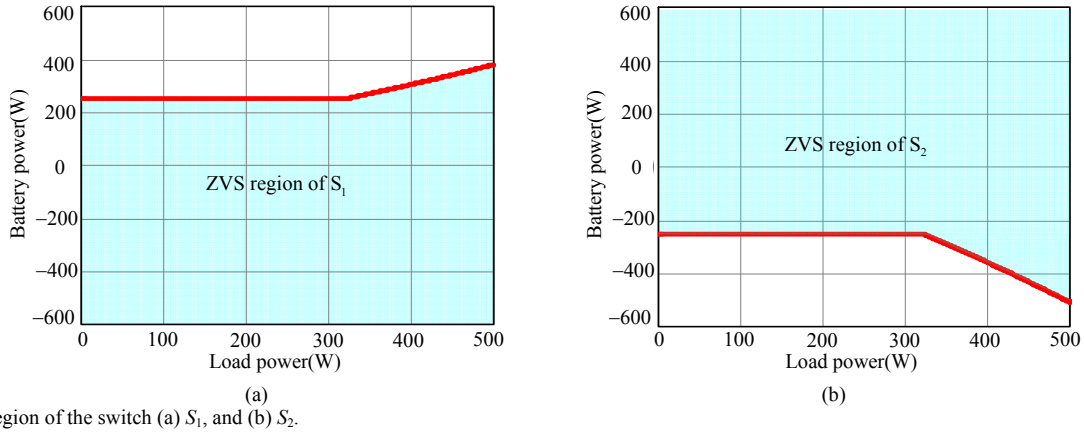

Fig. 14. ZVS region of the switch (a) S_1, and (b) S_2.

$$P_{o\_DCM1} = P_B \cdot \frac{4D^2(1-G)\pi^2 + 4\pi DG\varphi - G\varphi^2}{G^2\pi} \tag{20}$$

$$P_{o\_DCM2} = P_B \cdot \frac{\varphi^2}{2\pi G(G-1)} \tag{21}$$

It can be seen that the output power of the load port is a function of the duty cycle and the phase shift angle when the converter operates in the CCM and DCM1. Therefore, in the CCM and DCM1, the regulation of the load port is not fully decoupled with the primary-side power ports. In practice, the bandwidth of the load voltage control loop can be set much higher than that of the power control loops between the battery and the PV source in order to guarantee a fast response to variations in load. This method is straight forward to implement and can realize approximate decoupled control of the load port from the regulation of the battery and PV ports.

According to (13), (15) and (19)-(21), the normalized load power curves versus the secondary-side phase shift angle φ with different primary-side duty cycle D (the duty cycle of the upper switches S_1 and S_3) are plotted and shown in Fig. 13. It can be seen that, for a given G and phase shift angle φ, the output power in the CCM is greater than that in the DCM1, while the output power in the DCM1 is greater than that in the DCM2. The normalized voltage gain can either be lower than 1 or greater than 1. However, if G<1, the minimum output power P_{omin} cannot reach zero when φ=0. Besides, the operation region of the DCM1 is highly dependent on the primary side duty cycle. The operation region of the DCM1 decreases when the primary side duty cycle approaches to 0.5. There is no DCM1 when the primary-side duty cycle is equal to 0.5. Due to the symmetry of the primary side full-bridge circuit, the load power characteristics of the FB-TPC with duty cycle greater than 0.5 are the same as the situations with duty cycle smaller than 0.5. Substituting the D with (1-D) in (19)-(21), the output characteristics when D>0.5 can be derived.

B. *Soft-Switching Characteristics*

1) Secondary-Side Switches

According to the operation principles of the converter, the body diodes of the secondary-side switches, S_5 and S_6, always conduct before applying gating signals no matter which mode the converter works in. That means the drain-source voltages of S_5 and S_6 have decreased to zero before applying gating signals. Therefore, ZVS can be achieved for the secondary-side switches. Meanwhile, the changing rates of the currents through rectifying diodes D_1 and D_2 are limited by the inductor L_f. So the currents of D_1 and D_2 always decrease to zero slowly, which means ZCS is achieved. So the main power losses of the rectifying diodes are conduction losses. The conduction loss of each diode is ($V_F \cdot I_o$), where V_F is the forward voltage of the diode and I_o is the average load current. In summary, soft switching performance of the secondary-side devices is independent on the operation mode, and can be achieved within the entire operating range.

2) Primary-Side Switches

Due to the symmetry of the primary-side circuit, the ZVS conditions of S_1 and S_3 are the same, while ZVS conditions of S_2 and S_4 are the same. Therefore, only ZVS conditions of the switches S_1 and S_2 are analyzed here.

If the body diode of the primary-side switch is in ON state and the drain-source voltage has decreased to zero before its driving signal is applied, then ZVS is achieved. In order to realize ZVS, the current flowing through the corresponding switch should be negative when the switch is turned-ON. Therefore, the ZVS performance of S_1 and S_2 is determined by the currents flowing through the primary-side inductor L_1 and the secondary-side Boost inductor L_f. According to the operation principles and the reference directions of L_1 and L_f, we have

$$\begin{cases} i_{S1}(t) = i_{L1}(t) + n i_{Lf}(t) \\ i_{S2}(t) = -[i_{L1}(t) + n i_{Lf}(t)] \end{cases} \tag{22}$$

Therefore, the detailed constraints for ZVS of the switches S_1 and S_2 can be given by the following equations.

$$\begin{cases} S_1 : i_{L1}(t_{S1}) + n i_{Lf}(t_{S1}) < 0 \\ S_2 : i_{L1}(t_{S2}) + n i_{Lf}(t_{S2}) > 0 \end{cases} \tag{23}$$

where t_{S1} and t_{S2} are the turn-ON time of switches S_1 and S_2, respectively.

As shown in Fig.6, the current of L_1, i_{L1}, is given by the following equations.

$$\begin{cases} i_{L1}(t_{S1}) = \dfrac{P_{BAT}}{2V_{BAT}} - \dfrac{1}{2}\cdot\dfrac{V_{BAT}}{L}\cdot(1-D)T_s \\ i_{L1}(t_{S2}) = \dfrac{P_{BAT}}{2V_{BAT}} + \dfrac{1}{2}\cdot\dfrac{V_{BAT}}{L}\cdot(1-D)T_s \end{cases} \tag{24}$$

According to the operation principles of CCM and the waveforms shown in Fig.7, and ignoring the influence of dead-time, the ZVS conditions of S_1 and S_2 in CCM can be given by:

$$\begin{cases} S_1 : \dfrac{P_{BAT}}{2V_{BAT}} - \dfrac{1}{2}\cdot\dfrac{V_{BAT}}{L}\cdot(1-D)T_s < -n i_{Lf}(t_0) \\ S_1 : \dfrac{P_{BAT}}{2V_{BAT}} + \dfrac{1}{2}\cdot\dfrac{V_{BAT}}{L}\cdot(1-D)T_s > -n i_{Lf}(t_4) \end{cases} \tag{25}$$

Similarly, according to the operation principles of DCM1 and the waveforms shown in Fig.9, the ZVS conditions in DCM1 are given by:

$$\begin{cases} S_1 : \dfrac{P_{BAT}}{2V_{BAT}} - \dfrac{1}{2}\cdot\dfrac{V_{BAT}}{L}\cdot(1-D)T_s < 0 \\ S_1 : \dfrac{P_{BAT}}{2V_{BAT}} + \dfrac{1}{2}\cdot\dfrac{V_{BAT}}{L}\cdot(1-D)T_s > -n i_{Lf}(t_3) \end{cases} \tag{26}$$

According to the operation principles of DCM2 and the waveforms shown in Fig.11, the ZVS conditions in DCM2 are given by:

$$\begin{cases} S_1 : \dfrac{P_{BAT}}{2V_{BAT}} - \dfrac{1}{2}\cdot\dfrac{V_{BAT}}{L}\cdot(1-D)T_s < 0 \\ S_1 : \dfrac{P_{BAT}}{2V_{BAT}} + \dfrac{1}{2}\cdot\dfrac{V_{BAT}}{L}\cdot(1-D)T_s > 0 \end{cases} \tag{27}$$

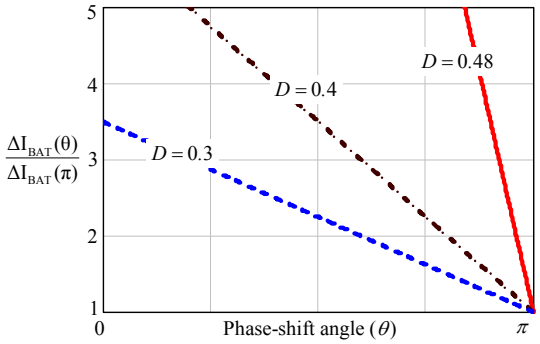

Fig. 15. Comparison of the current ripple on the battery port.

It is obvious that the ZVS performance is only determined by the battery power when the converter operates in DCM2.

To show the soft-switching performance, the ZVS margin of the proposed converter is plotted in Fig.Fig. 11, where a PV-battery hybrid power system is employed with the following parameters: V_{PV}=84V, V_{Bat}=42V, L_1=L_2=35μH, L_f=20μH, n=1.5, f_s=100kHz. In Fig.14, the converter only operates in the CCM and DCM2, because the duty cycle D is 0.5. It can be seen that when the battery is charged with P_{Bat}>0, ZVS of S_2 can be always achieved, whereas, ZVS of S_1 can be always achieved when the battery is discharged with P_{Bat}<0.

C. Current Ripple of the Battery Port

As mentioned above, the two bidirectional Buck/Boost converters on the primary side operate in an interleaved manner, which reduces the current ripple of the battery port. For a given duty cycle D with L_1= L_2= L, the current ripple of the two Boost inductors are ΔI_L. When the phase-shift angle between the two Buck/Boost converters is θ (0~π), the current ripple on the battery port ΔI_{BAT}, which is normalized with ΔI_L, can be given by the following equations.

$$\Delta I_{BAT}(\theta) = \begin{cases} 2(1-D-\theta/2\pi)/(1-D), & D \le 0.5 \\ 2(D-\theta/2\pi)/D, & D > 0.5 \end{cases} \tag{28}$$

For the proposed FB-TPC, the phase-shift angle between the two Buck/Boost converters is constant and equal to π. However, for the full-bridge TPCs presented in [20]-[24], the primary-side phase shift angle is used to regulate the output voltage and varies from 0 to π. The comparison of the current ripples between the proposed FB-TPC and previously presented FB-TPCs is illustrated in Fig.15, where it is shown that the current ripple can be significantly reduced with the proposed FB-TPC.

D. Design Consideration

1) As Turns Ratio of Transformer

The design criterion for the turns ratio of the transformer is to make sure that the load voltage can be regulated within the entire PV voltage range. Since the secondary-side circuit of the FB-TPC is a bridgeless Boost rectifier, the turns ratio n of the transformer is determined by the maximum PV voltage V_{PVmax}, the minimum voltage gain G_{min} when φ=0, and the output voltage V_o.

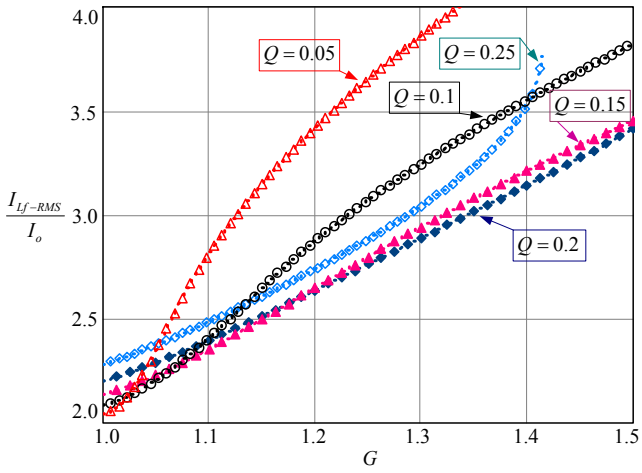

Fig. 16. Normalized L_f RMS current versus normalized voltage gain with different characteristic factors.

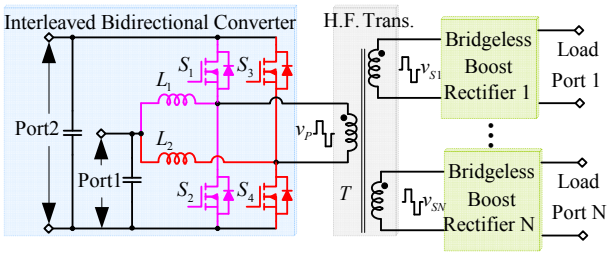

Fig. 17. Configuration of multiport converter based on the bridgeless Boost rectifiers.

$$n = \frac{V_o}{2V_{PV\max}G_{\min}} \tag{29}$$

As indicated by Fig.13, G_{min} is determined by the minimum load power when φ=0. Specially, G_{min} =1 if the load power can be as low as zero when φ=0.

2) Inductor L_f of the Bridgeless Boost Rectifier

Since soft-switching of the power devices on the secondary-side is achieved within the entire operating range, reduction of the conduction loss is the main consideration for designing L_f. In order to estimate the conduction losses, the root-mean-square (RMS) current of L_f , $I_{Lf\text{-}RMS}$, is calculated and normalized by the load current I_o. The curves of the normalized $I_{Lf\text{-}RMS}$ are shown in Fig. 16, where Q is the characteristic factor and defined as follows:

$$Q = \frac{16L_f f_s}{R_o} \tag{30}$$

As shown in Fig.16, when G is approached to 1, lower conduction loss can be achieved with a smaller Q. However, if Q=0.05, 0.1 or 0.25, higher conduction loss occurs as G increasing. On the other hand, when Q is in the range of 0.15~0.2, lower RMS current can be achieved within a wide operating range. Meanwhile, the RMS current and conduction loss is not sensitive to the value of L_f when Q is in the range of 0.15~0.2. Taking these factors into consideration, it is recommended to design the Q in the range of 0.15~0.2. For a design example with f_s=100kHz, P_o=500W, and V_o=300V, Q=0.15~0.2 means the value of L_f is in the range of 16.8μH~22.5μH.

3) Primary-side Inductors and Power Devices

The design of the primary side filter inductor and selection of power devices are the same as traditional power converters. The two primary filter inductors L_1 and L_2 are designed according to the inductor current ripple. There are two considerations for selecting power devices. One consideration is the current and voltage stresses. The voltage stresses of primary-side MOSFEs are equal to the PV voltage, the voltage stresses of rectifying diodes are equal to the load voltage, while the voltage stresses of the secondary-side switches is only half of the load voltage. The other one consideration is the reduction of conduction losses. Since the voltages of the primary-side PV source and battery are low and soft-switching is achieved, the reduction of conduction loss is one of the major considerations for power device selection. So power MOSFETs with low ON-resistance is preferred.

E. Topology Extension

An advantage of the proposed TPC derivation method is that the number of the isolated load port can be extended easily to interface multiple loads. This can be realized by using a multi-winding transformer and multiple bridgeless Boost rectifiers. The configuration of the proposed multiport converter with multiple isolated output ports is shown in Fig.17. The topology of the bridgeless Boost rectifier can be selected from those shown in Fig. 2 according to the requirement of practical application. The topology extension and control principles of the proposed multiport converter are similar to the existing multiport converters based on multi-winding transformer [10]-[12]. The output voltage/power of each load port can be regulated by phase shifting the driving signals of the active switches in each bridgeless Boost rectifier with respect to the primary-side switches. Since the output power of each load port is only determined by the phase-shift angle of its own bridgeless Boost rectifier, independent regulation of each load port can be achieved.

V. Experimental Results

A digital-controlled 800W prototype is built to verify the theoretical analysis. The converter is designed for a spacecraft power system, which is a typical stand-alone renewable power system. The specifications are listed in Table I.

Fig.18 shows the steady-state waveforms of the primary-side circuit in the proposed FB-TPC when the battery is charged. It can be seen that the total current ripple on the battery port has been significantly reduced by operating the two bidirectional converter in an interleaving manner. The waveforms of voltage v_{AB} between the midpoints the primary-side full-bridge, voltage v_{CD} between the midpoints of the secondary bridge, and the current i_{Lf} of the secondary-side inductor under different operation modes are shown in Fig. 19. Waveforms in Fig. 19(a) are tested when the converter operates in the CCM, where continuous inductor current i_{Lf} can be seen. Fig. 19(b) and 19(c) are corresponding waveforms of DCM1 and DCM2, respectively. It can be seen that when the converter operates in the CCM, the inductor current decreases to zero when the secondary-side voltage v_{CD} is zero and the primary-side voltage v_{AB} is not zero, which means the primary side switches commute before the secondary side inductor current, i_{Lf},

TABLE I KEY PARAMETERS OF THE PROTOTYPE

Components	Parameters
Input voltage of PV (V_{PV})	70V~100V
Voltage of battery (V_{BAT})	42V
Output voltage (V_o)	300V
Maximum PV power (P_{PV})	800W
Maximum output power (P_o)	500W
Switching frequency (f_s)	100kHz
Turns ratio of transformer (n)	1.5
Inductor (L_f)	20μH
Inductor (L_1, L_2)	35μH
Primary-side MOSFETs (S_1~S_4)	IPP075N15N3 G
Secondary-side MOSFETs (S_5~S_6)	IXTQ 82N25P
Secondary-side diodes (D_1~D_2)	DSEC 30-06A
Digital signal processor (DSP)	MC56F8247

decreases to zero. When the converter operates in the DCM1, the inductor current decreases to zero when the primary-side voltage v_{AB} is still in zero state, which means the two upper switches or lower switches are ON when i_{Lf} reaches zero. When the converter operates in the DCM2, the inductor current has decreased to zero when the primary-side voltage v_{AB} is not zero, which means S_1 and S_4, or S_2 and S_3 are ON when i_{Lf} reaches zero. The waveforms in Fig.18 and Fig.19 satisfy the theoretical analysis pretty well.

The switching waveforms of the primary-side switches when the converter operates in the CCM are shown in Fig. 20. As shown in Fig. , ZVS is accomplished for the primary-side switches S_1 and S_2. Since the switches S_3 and S_4 operate in the same pattern, ZVS can also be accomplished for the primary-side switches S_3 and S_4. The soft-switching waveforms of the secondary-side switches S_5 and S_6 are shown in Fig. 21. In comparison with the primary-side switches, it is easier to achieve ZVS for the secondary-side switches. As indicated in Fig. 21, ZVS of the two secondary-side switches is achieved in both continuous current mode and discontinuous conduction mode.

In order to verify the effectiveness of the FB-TPC under closed-loop control, the power management and control strategies for a PV-battery power system presented in [18][22] are applied to the proposed FB-TPC. The power management of the PV-battery power system is to balance the power between the PV and the battery while maximizing the output power of the PV source. The control block diagram is shown in Fig.22. Four regulators, PV voltage regulator (IVR) for MPPT, battery voltage regulator (BVR) for maximum charging voltage control, battery current regulator (BCR) for maximum charging current control and output voltage regulator (OVR) for load voltage control, are employed to achieve the power management of the system. The detailed analysis and operating principles of the power management system have been presented in [18][22], and will not be analyzed here. The power control and modulation of the FB-TPC are realized using a digital signal processor. The transient waveforms with output load stepping up and stepping down are tested and shown in Fig. 23. It can be seen that when the output load steps, the battery switching between charging mode and discharging mode. It indicates that the input power is kept constant, and the output voltage is stable during the load transients, because the battery power varies automatically to compensate for the load power variation. The transient waveforms with PV power changing

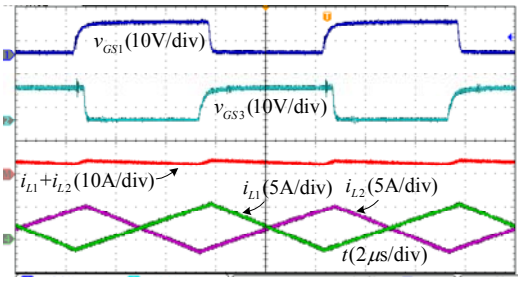

Fig. 18. The steady-state experimental waveforms of the primary-side interleaved bidirectional Buck/Boost converter.

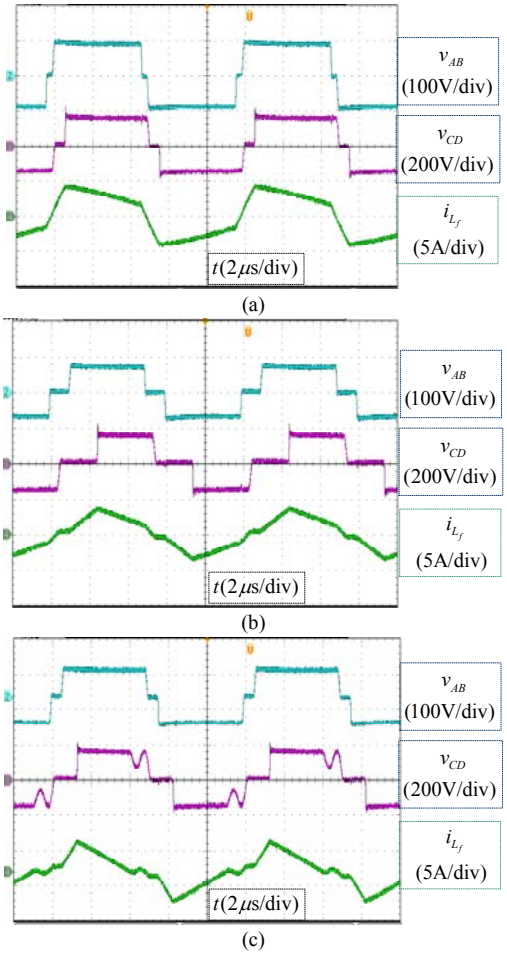

Fig. 19. The steady-state experimental waveforms of v_{AB}, v_{CD}, and i_{Lf} in: (a) CCM; (b) DCM1, and (c) DCM2.

are tested and shown in Fig. 24. A variable resistor in series with a dc source is used to emulate the PV source. The PV power is changed by adjusting the series resistor. It can be seen that the battery automatically balances the power between the PV and the load. The output voltage is stable when the PV power is changed. The tests indicate that power management of a three-port power system can be accomplished with the proposed FB-TPC.

The efficiencies, when the power is transferred from the PV to the battery, from the battery to the load, and from the PV to the load, are tested and shown in Fig.25(a). With the non-isolated Buck power conversion, the maximum efficiency

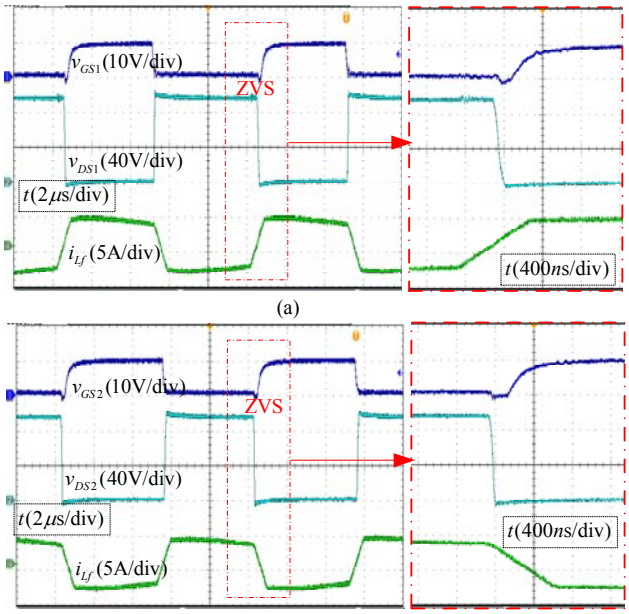

Fig. 20. Soft-switching waveforms of primary-side switches (a) switch S_1, (b) switch S_2.

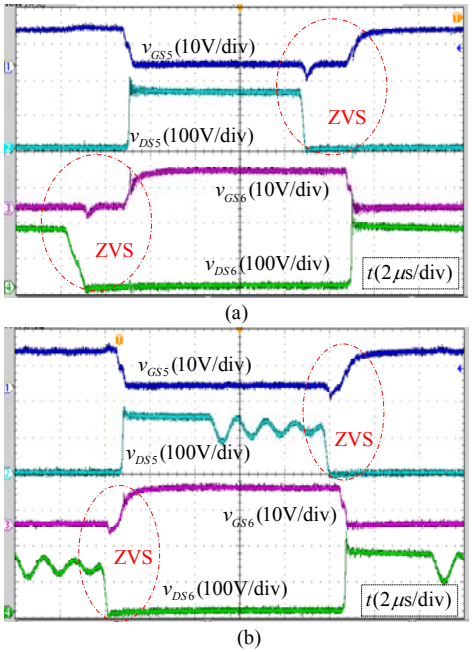

Fig. 21. Soft-switching waveforms of secondary-side switches S5 and S6 in (a) CCM, and (b) DCM2.

is about 97.6% at full-load when the power is transferred from the PV to the battery. When the power is transferred from PV to the load, the efficiency is 96%, and when the power is transferred from battery to the load, the efficiency is about 94.5% at full load. With single stage power conversion between any two of the three ports, high conversion efficiency within a wide load range is achieved. Fig. 25(b) shows the efficiency curve versus the battery power when the load-port is under full-load condition. In Fig. 25(b), the battery power varies from -550W to 350W, while the PV power varies from about 860W to 0W. It can be seen that the efficiency increases when the

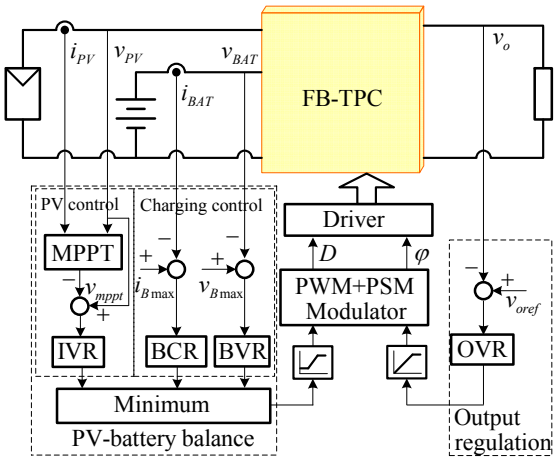

Fig. 22. Control block diagram of the FB-TPC.

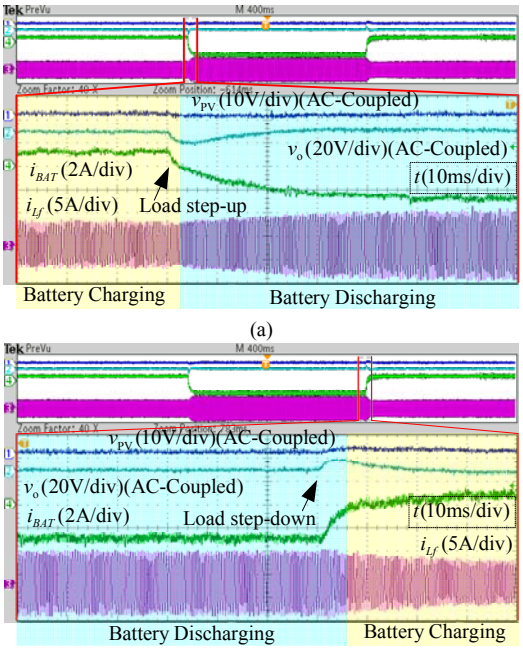

Fig. 23. Load transient waveforms, (a) load step-up, (b) load step-down.

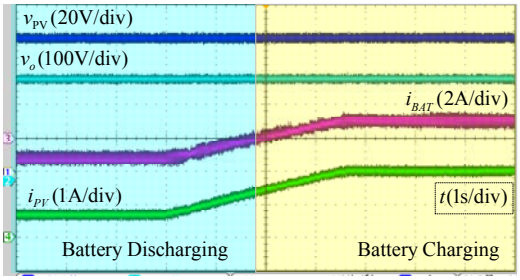

Fig. 24. PV power transient waveforms.

battery discharging power decreases and the charging power increases. It is because, as shown in Fig. 25(a), the charging efficiency is higher than the discharging efficiency.

In comparison with the full-bridge TPCs presented in [19]-[23], a major innovation of the proposed FB-TPC is that the conversion efficiencies from the primary-side power ports to the load port are improved. In [19], the efficiency versus battery

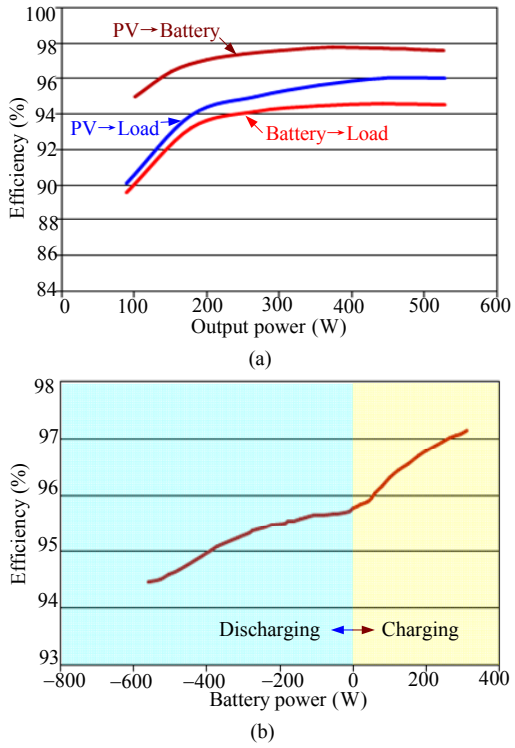

Fig. 25 (a) Efficiency curves of PV to battery, PV to load and battery to load, (b) efficiency versus battery power under full-load condition.

power under full-load condition is always lower than 94%. In [20] and [21], although soft-switching is achieved, the efficiency from PV to the load is only about 90%. In [22], the efficiencies from the primary-side power ports to the load port are always lower than 90%. In [23], the efficiency from battery to load is lower than 93% and the efficiency from PV to load is lower than 95%. It can be seen that these efficiencies in the previous full-bridge TPCs are all lower than the proposed FB-TPC.

VI. Conclusion

In this paper, a systematic method for synthesizing three-port converters (TPCs) from interleaved bidirectional converter and bridgeless Boost rectifiers has been proposed. The bidirectional converter and the bridgeless Boost rectifier are connected by a high-frequency transformer to interface multiple bidirectional sources and isolated output load simultaneously. Single-stage power conversion is realized to improve conversion efficiency of the power system. Voltage and power regulations over two of the three power ports are achieved by using interleaved pulse width modulation on primary-side switching-bridges and phase-shift modulation on secondary-side switches. Furthermore, soft-switching operation of all of the active-switches and diodes has been achieved. The voltage/current ripples are reduced thanks to the excellent performance of the proposed TPC topologies and modulation strategies. The voltage stresses of the devices are reduced because the voltages of devices are naturally clamped by the input and output voltages. These features make the proposed topologies good candidates for renewable power systems. A typical full-bridge TPC developed by the proposed method is analyzed with circuit operation principles, control strategies and characteristics presented. Experimental results of a 800W prototype have verified the feasibility and effectiveness of the proposed topology derivation method and the advantages of the derived TPC topologies.

VII. References

[1] T. Dragicevic, J. M. Guerrero, J. C. Vasquez, D. Skrlec, "Supervisory control of an adaptive-droop regulated DC microgrid with battery management capability," IEEE Trans. Power Electron., vol. 29, no. 2, pp. 695-706, Feb. 2014.

[2] L. H. S. C. Barreto, P. P. Praca, D. S. Oliveira Jr., R. N. A. L. Silva, "High-voltage gain boost converter based on three-state commutation cell for battery charging using PV panels in a single conversion stage," IEEE Trans. Power Electronics, vol. 29, no. 1, pp. 150-158, Jan. 2014.

[3] A. Kwasinski, "Quantitative evaluation of DC microgrids availability: effects of system architecture and converter topology design choices," IEEE Trans. Power Electron., vol. 26, no. 3, pp. 835-851, Mar. 2011.

[4] W. Jiang and B. Fahimi, "Multiport power electronic interface—Concept, modeling and design," IEEE Trans. on Power Electronics, vol. 26, no. 7, pp. 1890–1900, Jul. 2011.

[5] H. Tao, A. Kotsopoulos, J. L. Duarte, M. A. M. Hendrix, "Family of multiport bidirectional DC-DC converters," IEE Proceedings of Electric Power Applications, vol. 153, no. 3, pp. 451-458, 2006.

[6] H. Wu, K. Sun, S. Ding, Y. Xing, "Topology derivation of nonisolated three-port DC-DC converters from DIC and DOC," IEEE Trans. Power Electron., vol. 28, no. 7, pp. 3297-3307, July 2013.

[7] Y.-M. Chen, A. Q. Huang, X. Yu, "A high step-up three-port DC-DC converter for stand-alone PV/battery power systems," IEEE Trans. Power Electron., vol. 28, no. 11, pp. 5049-5062, Nov. 2013.

[8] L.-J. Chien, C.-C. Chen, J.-F. Chen, Y.-P, Hsieh, "Novel three-port converter with high voltage gain," IEEE Trans. Power Electron., vol. 29, no. 9, pp. 4693-4703, Sep. 2014.

[9] S. Rezaee, E. Farjah, "A DC-DC multiport module for integrating plug-in electric vehicles in a parking lot: topology and operation," IEEE Trans. Power Electron., vol. 29, no. 11, pp. 5688-5695, Nov. 2014.

[10] S. Falcones, R. Ayyanar, X. Mao, "A DC-DC multiport-converter-based solid-state transformer integrating distributed generation and storage," IEEE Trans. Power Electron., vol. 28, no. 5, pp. 2192-2103, May 2013.

[11] S. Y. Kim, H.-S. Song, K. Nam, "Idling port isolation control of three-port bidirectional converter for EVs," IEEE Trans. Power Electron., vol. 27, no. 5, pp. 2495-2506, May 2012.

[12] L. Wang, Z. Wang, H. Li, "Asymmetrical duty cycle control and decoupled power flow design of a three-port bidirectional DC-DC converter for fuel cell vehicle application," IEEE Trans. Power Electron., vol. 27, no. 2, pp. 891-904, Feb. 2012.

[13] Z. Wang, H. Li, "An integrated three-port bidirectional DC-DC converter for PV application on a DC distribution system," IEEE Trans. Power Electron., vol. 28, no. 10, pp. 4612-4624, Oct. 2013.

[14] G.-J. Su, L. Tang, "A multiphase, modular, bidirectional, triple-voltage DC-DC converter for hybrid and fuel cell vehicle power systems," IEEE Trans. Power Electron., vol. 23, no. 6, pp. 3035-3046, Nov. 2008.

[15] H. Hu, S. Harb, X. Fang, D. Zhang, Q. Zhang, Z. J. Shen, I. Batarseh, "A three-port flyback for PV microinverter applications with power pulsation decoupling capability," IEEE Trans. Power Electron., vol. 27, no. 9, pp. 3953-3964, Sep. 2012.

[16] H. Al-Atrash, F. Tian, I. Batarseh, "Tri-modal half-bridge converter topology for three-port interface," IEEE Trans. Power Electron., vol. 22, no. 1, pp. 341-345, Jan. 2007.

[17] H. Wu, R. Chen, J. Zhang, Y. Xing, H. Hu, and H. Ge, "A family of three-port half-bridge converters for a stand-alone renewable power system," IEEE Trans. on Power Electronic, vol. 26, no. 9, pp. 2697–2706, Sep. 2011.

[18] Z. Qian, O. Abdel-Rahman, H. Al-Atrash, and I. Batarseh, "Modeling and control of three-port DC/DC converter interface for satellite applications," IEEE Trans. on Power Electronic, vol. 25, no. 3, pp. 637–649, Mar. 2010.

[19] H. Wu, K. Sun, R. Chen, H. Hu and Y. Xing, "Full-bridge three-port converters with wide input voltage range for renewable power systems," IEEE Trans. on Power Electronic, vol. 27, no. 9, pp. 3965–3974, Sep. 2012.

[20] Y. Hu, W. Xiao, W. Cao, B. Ji, D. J. Morrow, "Three-port DC-DC converter for stand-alone photovoltaic systems," IEEE Trans. Power Electron., vol. 30, no. 6, pp. 3068-3076, June 2015.

[21] W. Li, C. Xu, H. Luo, Y. Hu, X. He, C. Xia, "Decoupling-controlled triport composited DC/DC converter for multiple energy interface," IEEE Trans. Ind. Electron., vol. 62, no. 7, pp. 4504-4513, July 2015.
[22] W. Li, J. Xiao, Y. Zhao, and X. He, "PWM plus phase angle shift (PPAS) control scheme for combined multiport dc/dc converters," IEEE Trans. Power Electron., vol. 27, no. 3, pp. 1479–1489, Mar. 2012.
[23] H. Wu, P. Xu, H. Hu, Z. Zhou, and Y. Xing, "Multiport converters based on integration of full-bridge and bidirectional DC-DC topologies for renewable generation systems," IEEE Trans. on Industrial Electronics, vol. 61, no. 2, pp. 856–869, Feb. 2014.
[24] D. Tollik, A. Pietkiewicz, "Comparative analysis of 1-phase active power factor correction topologies," 14th International Telecommunications Energy Conference, 1992, pp. 517-523.
[25] Y. Jang, M. M. Jovanovic, "A bridgeless PFC boost rectifier with optimized magnetic utilization," IEEE Trans. Power Electron., vol. 24, no. 1, pp. 85-93, Jan. 2009.
[26] A. B. Lange, T. B. Soeiro, M. S. Ortmann, M. L. Heldwein, "Three-level single-phase bridgeless PFC rectifiers," IEEE Trans. Power Electron., vol. 30, no. 6, pp. 2935-2949, June 2015.
[27] G. D. Szarka, B. H. Stark, S. G. Burrow, "Review of power conditioning for kinetic energy harvesting systems," IEEE Trans. Power Electron., vol. 27, no. 2, pp. 803-815, Feb. 2012.

Hongfei Wu (S'11, M'13) was born in Hebei Province, China, in 1985. He received the B.S. and Ph. D degrees in electrical engineering and power electronics and power drives from Nanjing University of Aeronautics and Astronautics (NUAA), Nanjing, China, in 2008 and 2013, respectively. From June 2012 to July 2012, he was a gust PhD student at Institute of Energy Technology, Aalborg University, Denmark.
Since 2013, he has been with the Faculty of Electrical Engineering, NUAA, and is currently a Associate Professor with College of Automation Engineering, NUAA. He has authored and co-authored more than 90 peer-reviewed papers published in journals and conference proceedings. He is the holder of more than 17 Patents. His research interests are power converters, distributed power generation and spacecraft power system.
Dr. Wu was the recipient of the Presentation Award at IEEE Energy Conversion Conference and Exposition 2011, and also the Outstanding Reviewer of IEEE Transactions on Power Electronics (2013).

Junjun Zhang was born in Jiangsu Province, China, in 1986. He received his B.S. degree in electrical engineering from Nanjing University of Aeronautics and Astronautics (NUAA), Nanjing, China, in 2010. He is currently working toward a Ph.D. degree in electrical engineering at NUAA.
His main research interests include topology and control of power converters, distributed power generation, and spacecraft power systems.

Xiaoqing Qin was born in Jiangsu Province, China, in 1990. She received the B.S. and M.S degree in electrical engineering from Nanjing University of Aeronautics and Astronautics (NUAA), Nanjing, China, in 2012 and 2015, respectively.
Her main research interests include topology and control of power converters.

Tiantian Mu was born in Jiangsu Province, China, in 1991. She received the B.S. degree in electrical engineering from Nanjing University of Aeronautics and Astronautics (NUAA), Nanjing, China. She is currently working toward the M.S. degree in electrical engineering at NUAA. Her research interests include topology and control of soft-switching dc-dc converters.

Yan Xing (M'03) was born in Shandong Province, China, in 1964. She received the B.S. and M.S. degrees in automation and electrical engineering from Tsinghua University, Beijing, China, in 1985 and 1988, respectively, and the Ph.D. degree in electrical engineering from Nanjing University of Aeronautics and Astronautics (NUAA), Nanjing, China, in 2000.
Since 1988, she has been with the Faculty of Electrical Engineering, NUAA, and is currently a professor with College of Automation Engineering, NUAA. She has authored more than 100 technical papers published in journals and conference proceedings and has also published three books. Her research interests include topology and control for dc-dc and dc-ac converters.
Dr. Xing is an Associate Editor of the IEEE Transactions on Power Electronics. She is a member of the Committee on Renewable Energy Systems within the IEEE Industrial Electronics Society.